ELSEVIER

Journal of Structural Geology 26 (2004) 885–903

JOURNAL OF STRUCTURAL GEOLOGY

www.elsevier.com/locate/jsg

The role of recrystallisation on the deformation behaviour of calcite rocks: large strain torsion experiments on Carrara marble

Auke Barnhoorn*, Misha Bystricky, Luigi Burlini, Karsten Kunze

Geologisches Institut, Sonneggstrasse 5, ETH-Zürich, CH-8092, Switzerland

Received 18 January 2003; received in revised form 16 September 2003; accepted 6 November 2003

Abstract

The rheological, microstructural and textural evolution of Carrara marble was studied during experimental deformation in torsion up to very large shear strains ($\gamma = 0.4–50$). Experiments were performed at constant angular displacement rates corresponding to shear strain rates of 6×10^{-5}–3×10^{-3} s^{-1}, a confining pressure of 300 MPa and temperatures of 500, 600 and 727 °C. Microstructures and crystallographic preferred orientations (CPO) were analysed using light microscopy and electron backscatter diffraction (EBSD). At all conditions deformation occurred dominantly by dislocation creep, even up to very large shear strains. After peak stresses ($\gamma \leq 2$), recrystallisation mostly by subgrain rotation caused weakening (5–20%), grain size reduction and a change in the CPO. A monoclinic CPO that formed at small strains at all temperatures evolved into two different large strain CPOs at different temperatures. At large strains, even after complete recrystallisation, the CPO continued to strengthen and a secondary foliation was formed at a steep angle to the shear zone boundary. This secondary foliation was continuously reset by both subgrain rotation and grain boundary migration recrystallisation and eventually overprinted the primary foliation. Misidentifying the primary and secondary foliations could result in misinterpretation of the applied strain field. More generally, information about the amount of strain is lacking for microstructures and CPOs of highly deformed ultramylonites.

Keywords: Calcite; Large strain; Torsion; Rheology; Weakening; Dislocation creep; Microstructure; Crystallographic preferred orientation; Electron backscatter diffraction; Dynamic recrystallisation; Oblique foliation; Steady-state

1. Introduction

Natural shear zones are relatively small domains where large amounts of strain concentrated. It is generally assumed that after an initial amount of deformation the shear zone will reach a steady-state configuration. During steady-state conditions, deformation mechanisms, stress levels and microstructures as well as crystallographic preferred orientations (CPO) should be dynamically stable, i.e. they should not change any further with strain under constant conditions and should be independent of the previous deformation history (Covey-Crump, 1994). Non-coaxial deformation is usually inferred as a prerequisite for steady-state in natural mylonites. However, most of the published mechanical properties of geological materials were obtained from coaxial deformation experiments carried out to relatively small amounts of strain (typically 20%). Coaxial deformation experiments on calcite were described by e.g. Griggs et al. (1960), Handin et al. (1960), Schmid et al. (1977), Walker et al. (1990) and Rutter et al. (1994) and specifically on Carrara marble by e.g. Rutter (1974, 1995) and Schmid et al. (1980). The maximum strains reached in these experiments are too small to result in steady-state deformation behaviour. Steady-state was also not achieved in large strain experiments on Carrara marble in extension (Rutter, 1998) and in approximate simple shear up to shear strains of three (Schmid et al., 1987).

The addition of a torsion set-up to the Paterson triaxial deformation apparatus allows deformation experiments to be performed in simple shear to even larger shear strains, comparable with several thousand percent of strain in compression experiments (Paterson and Olgaard, 2000). Large strain deformation studies in torsion have been conducted so far on polycrystalline monomineralic aggregates of calcite (Casey et al., 1998; Pieri et al., 2001a,b), olivine (Bystricky et al., 2000), anhydrite (Heidelbach et al., 2001), quartz (Schmocker et al., 2003) and magnesiowüstite

* Corresponding author. Tel.: +41-1-6323702; fax: +41-1-6321080.
E-mail address: auke.barnhoorn@erdw.ethz.ch (A. Barnhoorn).

0191-8141/$ - see front matter © 2004 Elsevier Ltd. All rights reserved.
doi:10.1016/j.jsg.2003.11.024

(Heidelbach et al., 2003). In these studies remarkable changes in rheology, microstructure and CPO were observed during deformation to maximum shear strains of $\gamma = 15$. Experiments to larger shear strains are needed to determine whether stress levels, microstructures and CPOs become dynamically stable or continue to evolve during ongoing deformation.

We report an experimental deformation study in torsion on Carrara marble extended to larger shear strains and a wider range of experimental conditions than performed by Pieri et al. (2001a,b), i.e. to lower temperatures and lower and higher strain rates. During experiments at lower temperatures different slip systems may be activated and dynamic recrystallisation processes may be suppressed. Consequently they may produce different types of large strain microstructures than those reported at higher temperatures. Particular attention was paid to the role of dynamic recrystallisation on the evolution of rheology, microstructure and CPO at large strains. The evolution of the shear stress with strain was correlated to the CPO and microstructural evolution to infer the cause of weakening.

2. Experimental methods

2.1. Deformation tests

The specimens were obtained from the same block of Carrara marble that was described by Pieri et al. (2001a). Cylindrical samples of 5–12 mm in length and 10 or 15 mm in diameter were cored and oven-dried at 120–130 °C and atmospheric pressure for at least 24 h before the tests. Each sample was inserted in a 0.25 mm thick and 15 mm inner diameter iron jacket (10 mm diameter and a thickness of ~0.4 mm for 500 and 600 °C tests). The experiments (Table 1) were conducted at 500, 600 or 727 °C, at 300 MPa confining pressure and at constant angular displacement rates corresponding to shear strain rates between 6×10^{-5} and 3×10^{-3} s^{-1} up to various final amounts of shear strain ($\gamma \approx 0.4$–50).

During torsion experiments (Fig. 1), approximate simple shear deformation occurs locally at any given position in the sample. The shear strain and the shear strain rate increase linearly from zero along the central axis of the sample to a maximum value at the outer diameter. Shear strain rates at any radius are calculated from the angular displacement rates using Eq. (3) in Paterson and Olgaard (2000). The experimental shear strains and shear strain rates in Table 1 are the maximum values at the outer radius of the sample, where most of the strength is supported. The response of the internal torque (M) to a variation in angular displacement rate ($\dot{\vartheta}$) gives the stress exponent (n). Assuming power-law creep with a stress exponent n, the internal torque is proportional to the shear stress (τ) at the sample radius (R) (Eqs. (10) and (12) in Paterson and Olgaard (2000)). As the proportionality factor depends on n by a term $3 + 1/n$, the conversion is not very sensitive to the precise value of n, especially if n is significantly greater than three. For an exponential flow law, the behaviour can be approximated by a power-law with a very high n. In this study, a constant stress exponent of 10 was always used for the conversion of the measured torque into shear stress (see also Section 3.1).

In order to determine the amount of torque supported by the iron jacket during the experiments, calibration experiments on solid samples of low carbon steel were performed at equivalent conditions to the ones used in this study. Flow laws for iron were determined and the strength of the jacket was calculated for every experiment (~9, 6 and 1% of the sample strength for 500, 600 and 727 °C, respectively). The shear stress values were corrected for the strength of the iron jacket. The resolution in the internal torque ($\Delta M = 0.2$ Nm) corresponds to a shear stress resolution ($\Delta\tau$) of ± 0.25 MPa for 15 mm diameter samples and ± 0.8 MPa for 10 mm diameter samples (assuming a stress exponent of $n = 10$). The reproducibility of the stress values for experiments conducted at the same conditions was within 8 MPa. For the purpose of comparison, shear stress (τ) and shear strain rate ($\dot{\gamma}$) were converted into equivalent stress (σ) and strain rate ($\dot{\epsilon}$) for compression tests using the relationships $\sigma = \sqrt{3}\tau$ and $\dot{\epsilon} = \dot{\gamma}/\sqrt{3}$ in analogy to Schmid et al. (1987) and Paterson and Olgaard (2000). The temperature distributions were regularly calibrated so that the temperature variation across the sample was never more than 2 °C.

During experiments up to large shear strains, fluctuations of the measured internal torque were observed with a wavelength corresponding to 1 ± 0.05 complete revolution of the column. These fluctuations were interpreted to arise from minor misalignments of the column and were corrected using a sinusoidal torque–shear strain curve with a fixed period of one revolution and a fixed amplitude (maximum 2 Nm, corresponding to ~8 MPa for samples with a 10 mm diameter), which represents the average variation in torque. In the high temperature experiments (727 °C) these corrections produced a very flat and therefore stable torque value at large strains, whereas in the low temperature experiments (500 and 600 °C) other effects caused additional variations.

2.2. Microstructural analyses

Thin sections were made from the deformed samples for microstructural analysis. Since the amount of strain increases from the centre to the rim of the sample, thin sections were taken close to the rim of the cylinder and parallel to the cylinder axis (Fig. 1). In the middle of these sections the shear direction was parallel to the section cut. Both sides of the thin section were polished to a very fine polishing grade (0.05 μm alumina suspension) in order to obtain ultra-thin sections (1–5 μm thick). Two-dimensional grain size (diameter of a circle with equivalent area) histograms were calculated from grain boundary outline drawings based on light micrographs (mean value of number

Table 1
Experimental conditions and results of torsion experiments on Carrara marble. All experiments were performed at constant temperature, confining pressure and twist rate. The quoted shear strain rates are these at the rim of the sample. Strain rate stepping tests are not shown. Peak and large strain stresses are determined from the measured strain-internal torque curves (stress exponent $n = 10$ is assumed for torque to stress conversion, as described in detail in Paterson and Olgaard (2000)). The amount of recrystallisation was determined from ultra-thin sections and divided into five classes: (1) none (0% volume fraction), (2) minimal (1–35%), (3) minor (35–65%), (4) major (65–90%), and (5) complete (90–100%). The recrystallised grain sizes are calculated from digital grain boundary drawings as two-dimensional equivalent diameters and represent the mean values of the grain size histograms (in number fractions)

Experiment	Sample		Temperature (°C)	Shear strain rate (s^{-1})	Shear strain maximum	Peak stress (MPa)	Large strain stress (MPa)	Weakening (%)	Amount of recrystallisation	Recrystallisation mechanisms[a]	Recrystallised grain size (μm)	Comments
	Length (mm)	Diameter (mm)										
PO262	11.16	9.90	500	9×10^{-5}	1.5	165	–	–	None	–	–	
PO254	10.70	9.89	500	3×10^{-4}	1.4	163	–	–	None	–	–	Slip > leak
PO258	9.52	9.90	500	1×10^{-3}	2.1	176	–	–	None	–	–	
PO259	12.31	9.90	500	9×10^{-5}	3.6	155	146	5	Minimal	B	2.7	
PO280	11.61	9.84	500	1×10^{-3}	4.1	193	180	6				Sample fractured parallel to developed foliation
PO256	9.00	9.90	500	1×10^{-3}	5.0	181	170	5	Minimal	B		
PO260	11.72	9.92	500	3×10^{-4}	5.3	187	178	5	Minimal			Stepping strain rate and stepping temperature test
PO255	11.06	9.91	500	3×10^{-4}	6.0	177	169	4	Minimal	B		
PO323	5.08	9.89	500	1×10^{-3}	7.3	186	173	7				Sample fractured parallel to developed foliation
PO286	11.69	9.88	500	1×10^{-3}	13.5	178	168	5	Major	B + SR	2.5	
PO311	11.79	9.88	500				–	–		–	–	One hour pre-heating, no deformation
PO306	11.54	9.89	600	6×10^{-5}	2.2	103	–	–	Minimal	B	4.7	Small slip at $\gamma = 0.05$
PO307	12.20	9.87	600	3×10^{-4}	5.3	122	112	7	Minimal	B + SR	4.5	One hour pre-heating
PO346	5.30	9.88	600	2×10^{-3}	6.3	142	142	0				
PO287	11.45	9.92	600	1×10^{-3}	11.6	129	111	13	Major	B + SR	4.2	
PO348	5.42	9.89	600	2×10^{-3}	36.5	166	142	14		B + SR	4.1	
PO344	11.16	14.80	727	3×10^{-4}	0.4	72	–	–		–	–	
PO298	10.95	14.79	727	6×10^{-5}	0.6	50	–	–	Minimal	–	–	
PO266	10.11	14.75	727	2×10^{-3}	0.8	72	–	–	None	–	–	Slip → leak
PO264	10.17	14.71	727	6×10^{-5}	3.4	52	47	9	Minor	SR + GBM	10	Did not reach steady-state, stepping strain rate test
PO422	10.77	14.82	727	3×10^{-4}	5.0	57	41	27	Major	SR + GBM		
PO263	10.13	14.70	727	3×10^{-4}	5.2	59	47	20		SR		
PO362	11.07	14.77	727	3×10^{-4}	5.2	62	46	26	Major	SR + GBM		
PO267	10.17	14.76	727	2×10^{-3}	5.3	71	58	25	Major	SR + GBM	7	
PO274	10.11	14.77	727	3×10^{-4}	6.9	60	45	26	Complete			Stepping strain rate test, with Platinum foil around sample
PO303	10.12	14.77	727	1×10^{-3}	7.9	64	51	21	Complete			Stepping strain rate test
PO265	10.21	14.75	727	2×10^{-3}	10.6	77	59	23	Complete	SR	6	
PO222	6.12	14.69	727	3×10^{-3}	29.1	87	71	18	Complete	SR + GBM	6 + 18	
PO352	2.38	14.81	727	2×10^{-3}	50.2	79	64	19	Complete	SR + GBM	6 + 10	Jacket failure at $\gamma = 50$

[a] B = bulging, SR = subgrain rotation, GBM = grain boundary migration.

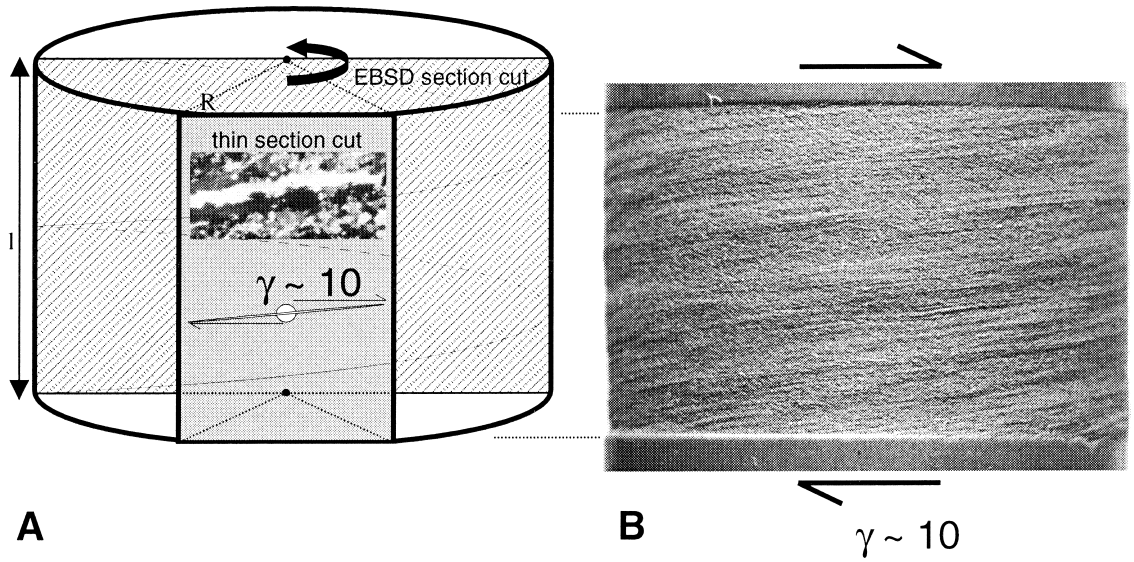

Fig. 1. (A) Schematic drawing of a torsion sample. Thin sections for microstructural analyses were cut at the outside rim of the sample, where the largest amount of shear strain occurs. In such a section, a circle (before deformation) is stretched into an ellipse and the long axis of the shear ellipse rotates towards the horizontal with increasing strain (shown here for $\gamma = 10$). A representative calcite microstructure deformed to $\gamma = 10$ shows a foliation in the same orientation as the theoretical shear ellipse (not to scale). During torsion experiments to large shear strains the sample makes several revolutions, as indicated by the black spiral line. EBSD sections were cut through the centre of the sample. (B) Carrara marble sample PO265 deformed in torsion to $\gamma \sim 10$. Small grooves in the iron jacket are visible parallel to the formed foliation and indicate the amount of shear strain. Shear sense is dextral. The diameter of the sample is 15 mm, the length is ~10 mm.

fraction histograms were used). No correction for cut effects was applied so that it was easy to compare the results with previous work. The auto-correlation function add-on (Panozzo Heilbronner, 1992) of the public domain NIH Image software was used for the analysis of shape preferred orientations (SPO), in particular to quantify the orientation of the primary and secondary foliation. This auto-correlation function quantifies size, symmetry and anisotropy of grains or clusters of grains as average properties of the microstructure.

2.3. Electron backscatter diffraction

Automated electron backscatter diffraction (EBSD) analyses (Venables and Harland, 1973; Adams et al., 1993) of the deformed samples were performed in a CamScan CS44LB scanning electron microscope (SEM) on samples cut as described above or in a plane parallel to the cylinder axis through the centre of the sample. The bulk samples were mechanically polished (down to 0.05 μm particle size) and lapped for 1 h with an alkaline colloidal silica suspension (particle size 25 nm). Lapped samples were coated with a ~4 nm carbon layer. The complete samples, apart from the lapped surface, were covered with silver paint in order to reduce charging in the SEM. The SEM working conditions used for EBSD analyses were: 15 kV acceleration voltage, 23 mm working distance, ~3 nA beam current and 70° sample tilt. The step sizes (20 μm for highly recrystallised samples and 100 μm for non-recrystallised samples) of the automated EBSD analyses were large enough so that any grain was measured at most once in order to maintain non-correlated orientation statistics. Additional high-resolution orientation imaging maps were obtained on section cuts from the outer rim of the samples using a step size of 2 μm. EBSD analyses in the centre parts of large strain samples gave similar pole figures to analyses close to the rim of small strain samples. The EBSD patterns were collected, indexed and analysed with the commercial TSL software OIM 3.0™. The analyses show a large number of data (usually 50–70%) with a high reliability (confidence index > 0.2). Recorded data with lower confidence indices were not used for the CPO analyses. The orientation distribution function (ODF) and contoured pole figures for the representation of the EBSD measurements were calculated using the program Beartex (Wenk et al., 1998). Contouring of the discrete data was carried out with a smoothing of 15° Gaussian width. The texture index J determined for the finite number of orientation data is extrapolated to that of an infinitely large data set according to Matthies and Wagner (1996) and Schmocker (2002).

3. Results

3.1. Mechanical behaviour

All the experiments (Table 1) showed similar shear stress–shear strain behaviours (Fig. 2). They were characterized first by an increase in shear stress towards peak values. The strain at which the peak stress was reached decreases with increasing temperature ($\gamma \approx 2$ at 500 °C and $\gamma \leq 1$ at 727 °C). Stresses remained at peak levels for a

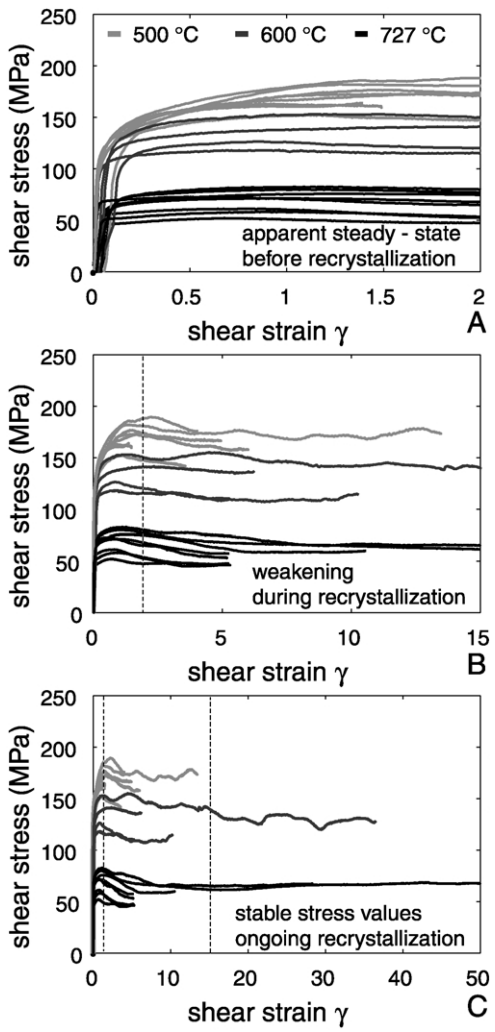

Fig. 2. Shear stress–shear strain diagrams for the torsion experiments performed on Carrara marble. The three diagrams show the same data in different strain ranges: (A) for $\gamma = 0$–2; (B) for $\gamma = 0$–15; and (C) for $\gamma = 0$–50. Shear stresses were converted from torque measurements assuming a stress exponent (n) of 10. Experiments were performed at constant shear strain rates between 6×10^{-5} and 3×10^{-3} s^{-1}. At any given temperature the experiments are reproducible and the apparent scatter in the data is mostly due to the difference in applied shear strain rates. At all temperatures the strength of the material increases as a function of shear strain rate. At $\gamma = 43$ in the largest shear strain experiment (727 °C) stepping test data was substituted by shear stresses interpolated from data before and after the stepping test. The stress–strain data of the large strain experiments ($\gamma > 15$) were corrected for sinusoidal fluctuations due to the experimental set-up.

shear strain interval of $\gamma \sim 0.5$–1 before weakening started (Fig. 2A). Slow weakening was observed at lower temperatures (~5% at 500 °C and ~12% at 600 °C both taken at $\gamma \sim 10$). The largest shear strain experiment at these conditions showed a very slow but continuous weakening (~18% between $\gamma = 2$ and 36 at 600 °C), suggesting that stable stress values were never reached. At 727 °C the weakening was more pronounced at moderate strains (~20% at $\gamma \sim 5$). After $\gamma = 5$ stress values remained approximately constant up to very large strains ($\gamma = 50$). At any given temperature, a systematic increase in strength was observed with increasing strain rate. Experiments performed at the same conditions were reproducible. Stress exponents determined with strain rate stepping tests were very high in all cases: $n \sim 20$ at 500 °C and $n \sim 7$–12 at 600 and 727 °C (Table 2). With increasing strain a small decrease in stress exponent was observed.

3.2. Microstructures

The undeformed Carrara marble consists of a well-equilibrated, homogeneous and coarse-grained microstructure. The calcite grains have equant shapes. The grain size distribution is unimodal with a mean 2D grain size of 125 μm. A small number of thin twins are present, but otherwise no internal deformation features occur. The CPO of the starting material is nearly random (Pieri et al., 2001a, b).

In the micrographs of the deformed samples some very thin and straight twins are visible. They are interpreted to be caused by rapid sample cooling after the deformation experiments and are not discussed any further.

3.2.1. 500 °C

Microstructures from the 500 °C experiments (Fig. 3) show abundant twins. A large number of relatively thin (~10 μm) bent twins formed at the start of deformation. The twins and grain boundaries stretched, bent and rotated with the imposed shear strain towards parallelism with the shear zone boundary (SZB). This caused the formation of a strong SPO. The onset of recrystallisation is marked by the appearance of a very small amount of small bulges and recrystallised grains (~2 μm) along the twin boundaries at $\gamma \geq 3$. At the largest shear strains ($\gamma \geq 10$) recrystallisation was more common along both grain and twin boundaries, although the highly elongated original calcite grains still dominate the microstructure. At large shear strains ($\gamma > 5$) brittle micro-fracturing occurred in combination with ductile deformation. In the sample deformed to $\gamma = 13$ a few small fractures in a Riedel-shear orientation were observed. These Riedel-shear fractures occurred on a small scale (~100 μm in length) and offset extensionally the foliation formed during ductile deformation. In addition,

Table 2
Stress exponents (n) for a power-law rate equation obtained from strain rate stepping tests for various temperatures and shear strains

Temperature (°C)	Shear strain range (γ)	Stress exponent (n)
500	1.5	24.9
	4	17.3
600	4	11.7
	4	11
	3	12.3
727	4	7.4
	5–7	6.8
	43	7.8

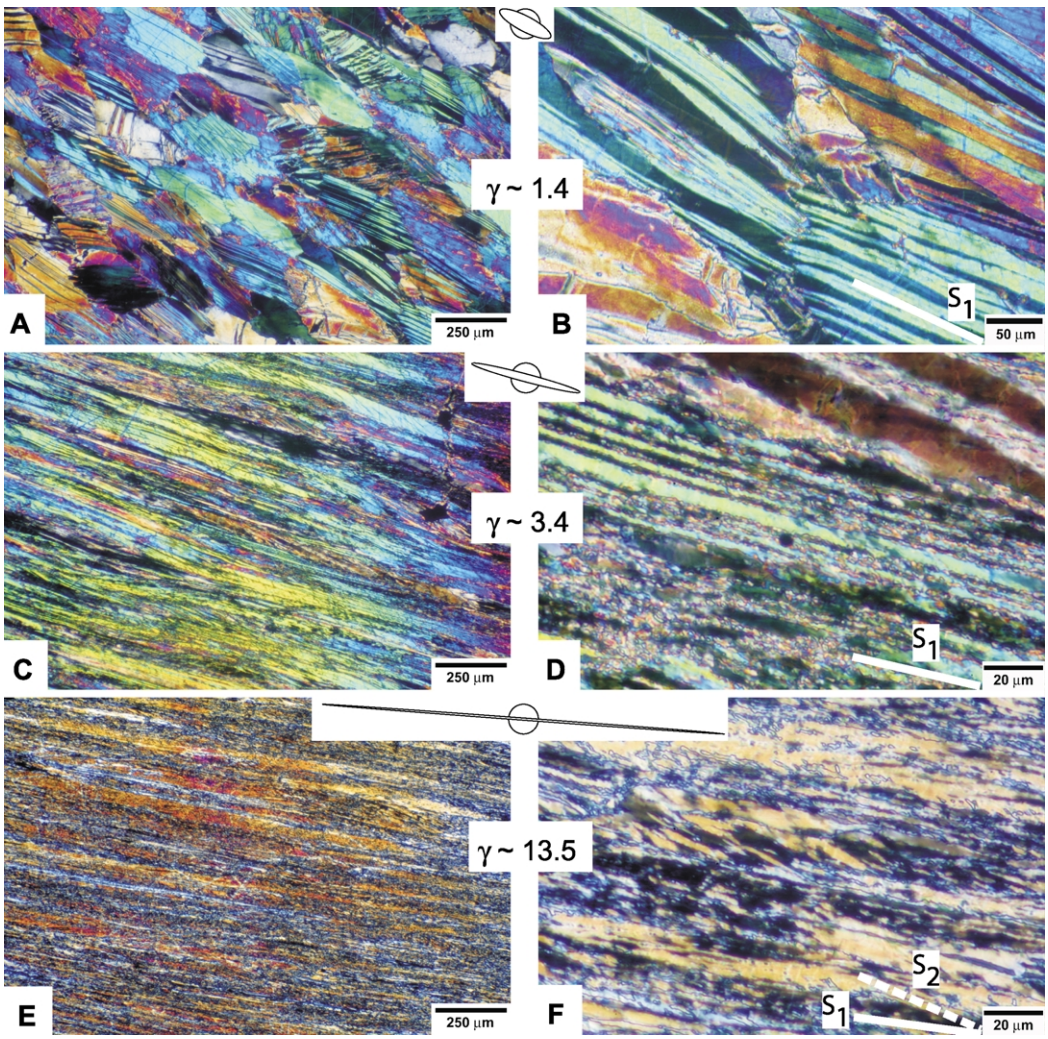

Fig. 3. Thin-section photographs in crossed-polarized transmitted light from samples deformed at 500 °C. Pairs from the same sample at low and high magnification are placed adjacent to each other. The sense of shear is sinistral. The orientation of the first and secondary foliations (S_1 and S_2) are indicated with white lines. A non-deformed circle and the simple shear ellipse are indicated for the specific shear strains. (A) and (B) Sample PO262, $\gamma = 1.4$ at 9×10^{-5} s^{-1}. The calcite crystals are heavily twinned and elongated. No recrystallisation is present at the twin and/or grain boundaries. (C) and (D) Sample PO259, $\gamma = 3.4$ at 9×10^{-5} s^{-1}. The calcite crystals are heavily twinned and highly elongated. Very small, recrystallised grains have developed mainly at twin boundaries. The change in colour from the left to right side of the photograph is caused by a difference in thickness of the section. (E) and (F) Sample PO286, $\gamma = 13.5$ at 1×10^{-3} s^{-1}. The calcite crystals are highly stretched. Some crystals cover the complete width of the thin-section. Original grain and twin boundaries cannot be distinguished. Small, recrystallised grains are formed along twin and grain boundaries. The amount of recrystallisation is about 70% of the sample.

they cut through long stretched grains. Several attempts to reach shear strains larger than 13 at 500 °C did not succeed due to brittle failure of the samples.

3.2.2. 600 °C

Similar deformation features were observed at small shear strains ($\gamma < 2$) at 500 and 600 °C. The twins were less numerous and thicker (~20 μm) at 600 °C (Fig. 4). They persisted in the microstructure until recrystallisation broke up the twinned calcite grains. At $\gamma = 2$ a small number of recrystallised grains were observed at the grain boundaries. The recrystallised grains were slightly larger than at 500 °C (~4 μm). At larger shear strains ($\gamma = 5$), subgrain rotation recrystallisation occurred at a large number of grain and twin boundaries. Small domains with two different sets of orientations of grain boundary alignments were formed (right bottom corner of Fig. 4D). They make an angle of ~20° with the main foliation and ~30° with the SZB. At a shear strain of $\gamma = 10$ a large part of the sample was recrystallised (~85% area fraction). The grain boundaries of the old elongated calcite grains were still recognisable in the microstructure. At even larger shear strains ($\gamma \sim 36$) the grain boundaries of the old elongated calcite grains vanished and a completely recrystallised microstructure formed.

3.2.3. 727 °C

At small strains, microstructures from samples deformed at 727 °C (Fig. 5) were characterized by the stretching and rotation of the calcite grains together with some twinning. The twins were thicker (~50 μm) and less frequent than at

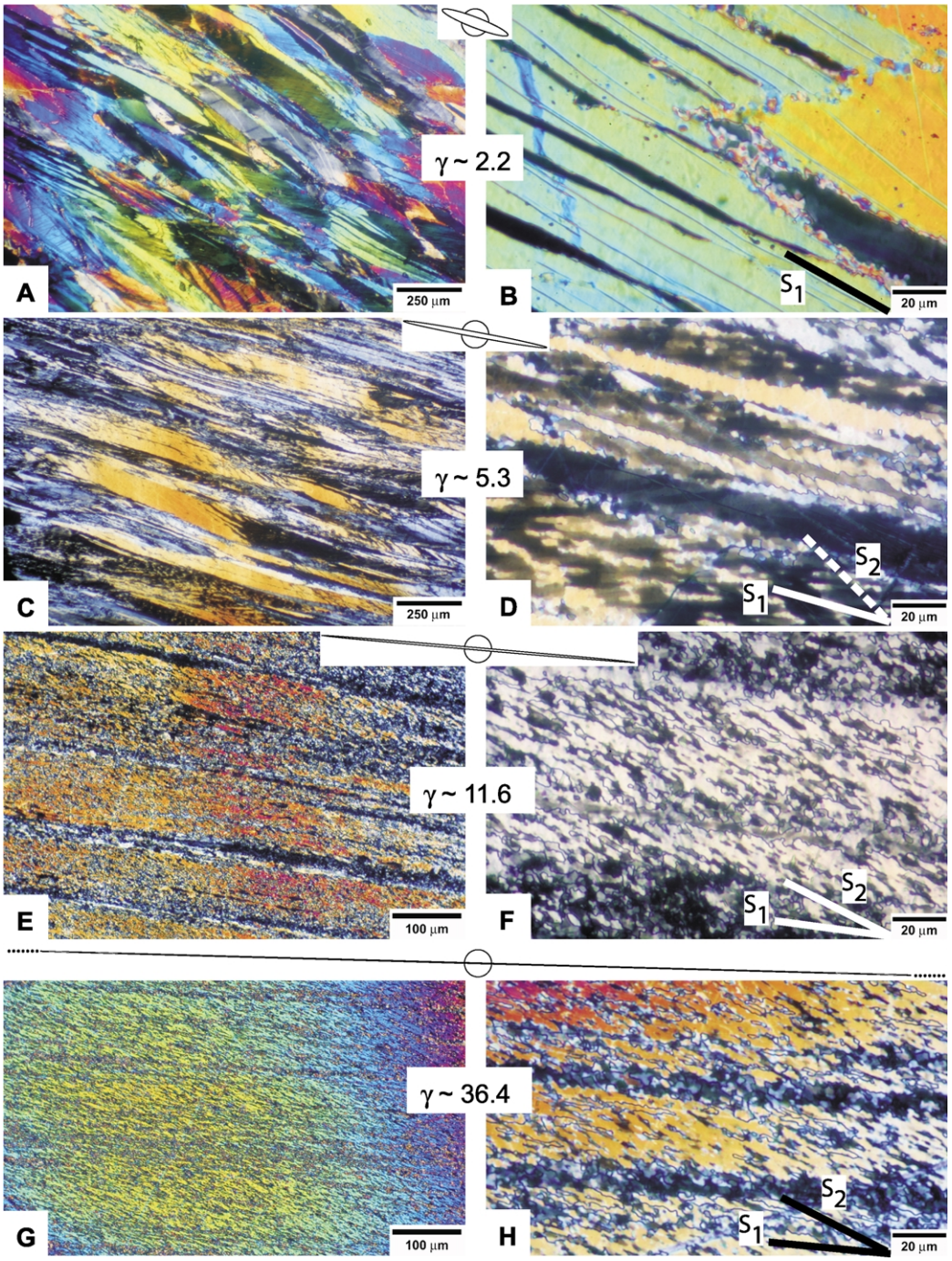

Fig. 4. Thin-section photographs in crossed-polarized transmitted light from samples deformed at 600 °C, presented as in Fig. 3. The orientation of the first and secondary foliations (S_1 and S_2) are indicated with white or black lines. (A) and (B) Sample PO306, $\gamma = 2.2$ at 6×10^{-5} s^{-1}. The calcite grains have twins, although they are less numerous and thicker than at the lower temperature (500 °C). Small, recrystallised grains start to form at the grain and twin boundaries. (C) and (D) Sample PO307, $\gamma = 5.3$ at 3×10^{-4} s^{-1}. Long stretched grains were formed. Inside these grains, subgrains are formed with steep grain boundaries with the sense of shear. Adjacent subgrains often have similar orientations (see bottom right corner of (D)). (E) and (F) Sample PO287, $\gamma = 11.6$ at 1×10^{-3} s^{-1}. A large part of the sample has recrystallised (about 85%). The boundaries of the original large stretched crystals are still visible. A secondary foliation with a steeper oblique orientation is also present. (G) and (H) Sample PO348, $\gamma = 36.4$ at 2×10^{-3} s^{-1}. The sample is completely recrystallised. The grain boundaries of the original stretched grains have vanished. A strong oblique secondary foliation between recrystallised grains is present.

lower temperatures and had a lensoidal shape. At $\gamma = 0.8$ irregular grain boundaries indicated incipient grain boundary migration recrystallisation. Elongated relict grains were still largely present at $\gamma = 3.3$, although a significant number of them were already divided and broken up. Recrystallisation was already pervasive. By $\gamma = 5.2$ the majority of the old calcite grains had recrystallised (75%) to a smaller grain size (around 10 μm). At $\gamma = 10$ the Carrara

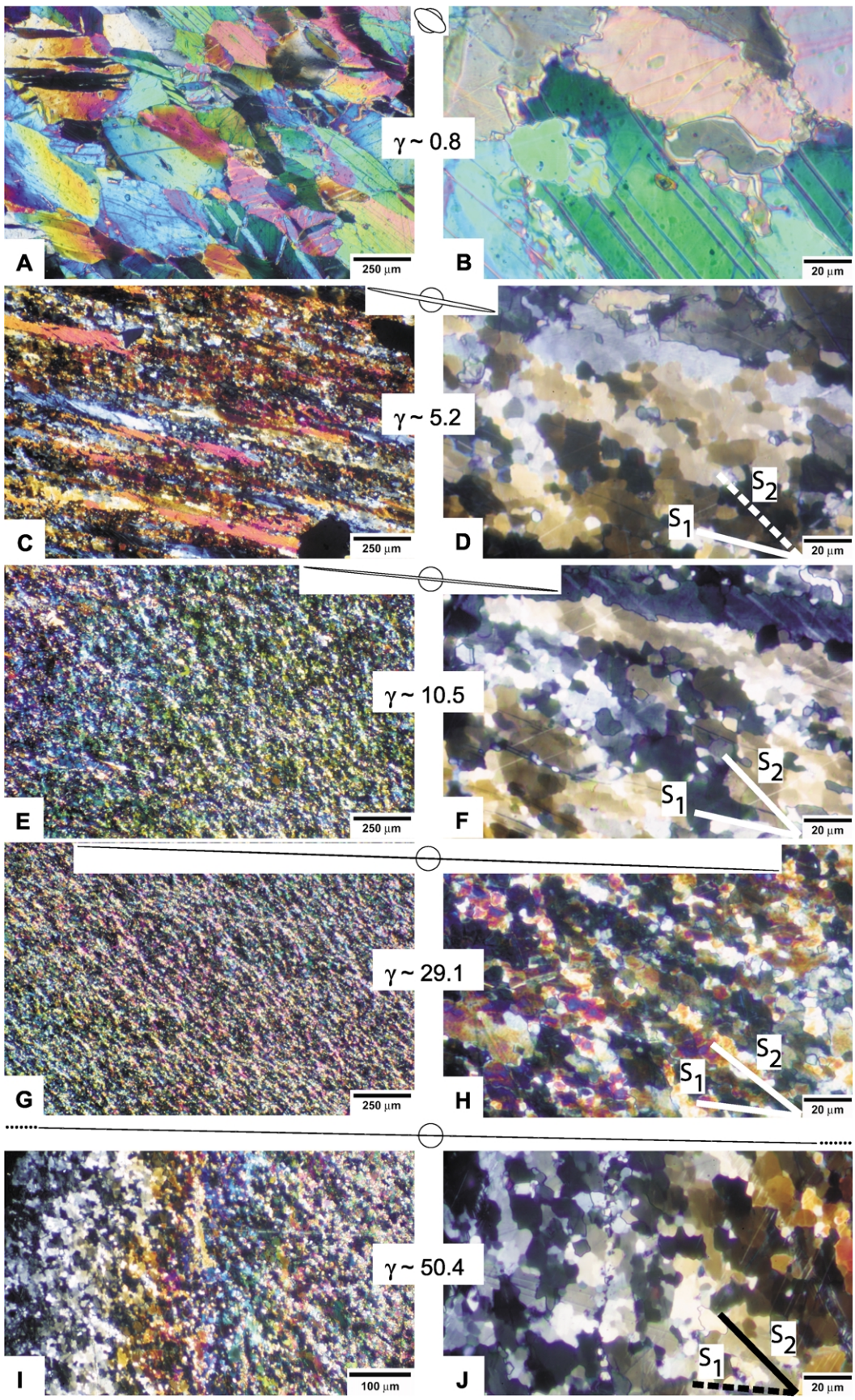
γ ~ 0.8
A
250 μm
B
20 μm
γ ~ 5.2
C
250 μm
D
S2
S1
20 μm
γ ~ 10.5
E
250 μm
F
S2
S1
20 μm
γ ~ 29.1
G
250 μm
H
S2
S1
20 μm
γ ~ 50.4
I
100 μm
J
S2
S1
20 μm

marble was completely recrystallised and a fine-grained calcite ultramylonite was formed. Subgrain rotation recrystallisation was the dominant recrystallisation process, but grain boundary migration recrystallisation was also observed. A steep secondary foliation formed oblique to the main foliation (angle ~ 50°) due to the alignment of the grain boundaries of the newly formed recrystallised grains. The secondary foliation was even more pronounced at larger strains ($\gamma = 29$ and 50), but the angle with the main foliation did not change significantly with strain (Fig. 6A). Irregular (lobate) grain boundaries and increased grain sizes indicated an increase in the importance of grain boundary migration recrystallisation at large shear strains ($\gamma > 10$). Around the larger grains, small-recrystallised grains aligned parallel to the secondary oblique foliation. The mean recrystallised grain size was larger (8–10 μm) than at lower temperatures and increased slightly to ~15 μm at larger shear strains ($\gamma = 29$). The grain size histogram clearly shows a bimodal grain size distribution with peaks at 8 and 20 μm (Fig. 6C).

3.2.4. Recrystallised grain size

Combining the recrystallised grain size data of the large strain experiments at all three temperatures resulted in a best-fit linear paleopiezometer (Fig. 6D) of:

$$\log\sigma = (-0.82 \pm 0.15)\log(d) + 2.73 \pm 0.11 \quad (1)$$

where σ is the equivalent stress in MPa and d is the equivalent 2D diameter of the recrystallised grains in μm. The analyses included both grains formed by subgrain rotation recrystallisation and grain boundary migration recrystallisation.

3.3. CPO

Two distinct evolutions of CPO with strain were observed in the deformed Carrara marble samples for low (500 and 600 °C) and high (727 °C) temperatures, respectively (Fig. 7).

At all temperatures investigated and at small amounts of shear strain ($\gamma < 4$) the CPO consists of two c-axis maxima, one oblique to the shear plane (40–45°) and opposite to the sense of shear and one perpendicular to the shear zone boundary (SZB, horizontal in the pole figures). The a-axis maxima form a girdle slightly tilted with respect to the SZB. One a-axis maximum is parallel to the shear direction and one of the r-pole maxima is perpendicular to the SZB. The CPO symmetry is monoclinic. For the low temperature experiments (500 and 600 °C) this CPO strengthens up to $\gamma \sim 6$ and at very large shear strains ($\gamma \geq 9$) a third c-axis maximum develops inclined to the SZB and oriented with the sense of shear. At $\gamma \sim 32$ this third maximum becomes dominant at 45° to the SZB, so that one {r} pole maximum is parallel to the SZB. With strain the pattern symmetry changes from monoclinic ($\gamma < 6$) to orthorhombic ($\gamma \sim 10$) and then again to monoclinic symmetry ($\gamma \sim 30$).

At higher temperatures (727 °C and higher; Pieri et al., 2001a) the CPO evolution differs from the low temperature one. With increasing strain the low strain CPO is replaced by a strong CPO with the c-axes normal to the shear direction and inclined about ±60° to the shear plane; i.e. orientation components between {r}⟨a⟩ and {c}⟨a⟩. One of the a-axis maxima is parallel to the shear direction. This CPO pattern does not change with strain any further even until very large strains ($\gamma = 50$), but it strengthens progressively. The large strain CPO resembles a very sharp single component CPO with orthorhombic symmetry. A small tail of c-axis orientations is situated next to the maxima with the sense of shear at both $\gamma = 29$ and $\gamma = 50$.

3.4. Secondary foliation

A detailed EBSD map of the sample deformed to $\gamma = 50$ at 727 °C (Fig. 8) clearly reveals a steep secondary foliation defined by a grain shape fabric at an angle of ~50° to the SZB (horizontal in Fig. 8). Using a colouring scheme of crystal axes normal to the SZB, the map (Fig. 8A) indicates a strong concentration of planes between {c} and {r} parallel to the SZB (yellow to red colours). The two strong orientation components between {r}⟨a⟩ and {c}⟨a⟩ are highlighted in blue and red in Fig. 8B, emphasizing that their mutual boundaries form the steep secondary foliation, extracted again in Fig. 8C. Misorientation analyses (Prior, 1999) reveal the orientation relationship (rotation axis and angle) between neighbouring measurements or grains. Two groups of misorientations dominate, one set of low angle misorientations (<20°) with randomly distributed rotation axes and another set of high angle misorientations with specific axes and angles. The second set of misorientations transforms the blue and red orientations into each other and is represented by six different angle/axis pairs with four distinct axes (Fig. 8D and Table 3). Of these representations the one with the smallest misorientation angle (78°) has its rotation axis aligned parallel to the trace of the secondary foliation. One of the {f} planes may be parallel to the secondary foliation assuming that the secondary foliation is

Fig. 5. Thin-section photographs in crossed-polarized transmitted light from samples deformed at 727 °C, presented as in Fig. 4. (A) and (B) Sample PO266, $\gamma = 0.8$ at 2×10^{-3} s^{-1}. A relatively small number of thick, lensoidal twins are present. Small, recrystallised grains have started to form at the grain boundaries. (C) and (D) Sample PO267, $\gamma = 5.2$ at 2×10^{-3} s^{-1}. Recrystallisation (~75%) is more pervasive. Some large stretched grains are still present, but most of them have been broken up by subgrain rotation recrystallisation. (E) and (F) Sample PO265, $\gamma = 10.5$ at 2×10^{-3} s^{-1}. The sample has completely recrystallised. A second steep foliation (S_2) formed by grain boundary alignment of the recrystallised grains. (G) and (H) Sample PO222, $\gamma = 29.1$ at 3×10^{-3} s^{-1}. This sample is also completely recrystallised and a second oblique foliation is present. (I) and (J) Sample PO352, $\gamma = 50.4$ at 2×10^{-3} s^{-1}. A steep second foliation is observed. No major evolution in microstructure is present between $\gamma = 10$ and $\gamma = 50$.

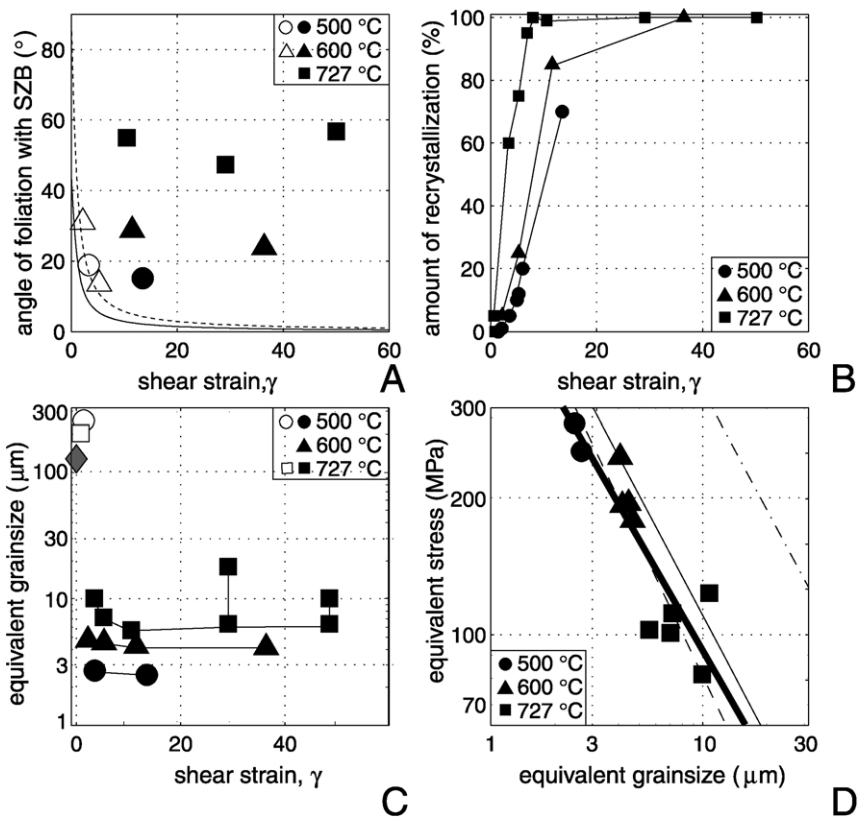

Fig. 6. (A) Orientation of the first and secondary foliations versus shear strain for the three temperatures. First and secondary foliations are represented as open and closed symbols, respectively. The dotted line represents the angle of an initially vertical line rotated during simple shear. The solid line represents the orientation of the long axis of the strain ellipse. The orientation of the first foliation should follow the orientation of the latter. (B) Percentage of recrystallised grains versus shear strain plotted for the three different temperatures. (C) Equivalent grain size versus shear strain for the non-recrystallised (open symbols) and recrystallised grains (black symbols). The grey symbol represents the grain size of the starting material. All plotted values are the 2D mean values of the grain size distribution histograms (number fractions). Two samples (727 °C, $\gamma \sim 30$ and $\gamma \sim 50$) show a bimodal grain size distribution histogram and both peak values are shown. (D) Log–log plot of differential stress versus recrystallised grain sizes. All plotted values are the 2D mean values of the grain size distribution histograms (number fractions). Shear stresses were multiplied by $\sqrt{3}$ for conversion to equivalent stresses. Paleopiezometers are shown for subgrain rotation recrystallised grains (solid line) and grain boundary migration recrystallisation (dash–dot line) from Rutter (1995) as well as for recrystallisation (dash–dash line) from Schmid et al. (1987) and from this study (black and thick line).

normal to the observation plane (section cut). Another {f} pole for both orientation components points parallel to a 180° rotation axis (in the pole figure centre). Thus, the misorientation is compatible with f-twinning between both components.

Table 3
List of the four different representations of the two dominant misorientations (between the blue and red grains in Fig. 8B and E) observed in sample PO352, $\gamma = 50$

Rotation angle	Rotation axis	
	⟨uvtw⟩ ∼	{hkil)
78.1°	$\langle 02\bar{2}1\rangle$ = s.d.	$\{01\bar{1}4\}$
134.9°	$\langle 80\bar{8}1\rangle$	$\{10\bar{1}1\}$ = h
180°	$\langle 04\bar{4}1\rangle$	$\{01\bar{1}2\}$ = f
180°	$\langle 10\bar{1}1\rangle$	$\{10\bar{1}8\}$ = x

4. Discussion

4.1. Effect of strain

Deformation of Carrara marble was essentially plastic, although some brittle features in the form of Riedel fractures were visible locally at large strains ($\gamma = 13$) at the lowest temperature (500 °C).

At all temperatures strain hardening occurred accompanied by intense twinning at small strains (Figs. 3–5). The thickness and number of twins vary with the applied shear stress and temperature (Burkhard, 1993). Because twinning can only account for a relatively small amount of shear strain in calcite ($\gamma_{max} = 0.68$, in the optimum single crystal orientation for calcite single crystals; Wenk, 1985), other mechanisms must be activated to accommodate large amounts of strain. The presence of undulous extinction, subgrains and new recrystallised grains with similar sizes to the subgrains suggest that Carrara marble mainly deforms by slip and climb of dislocations

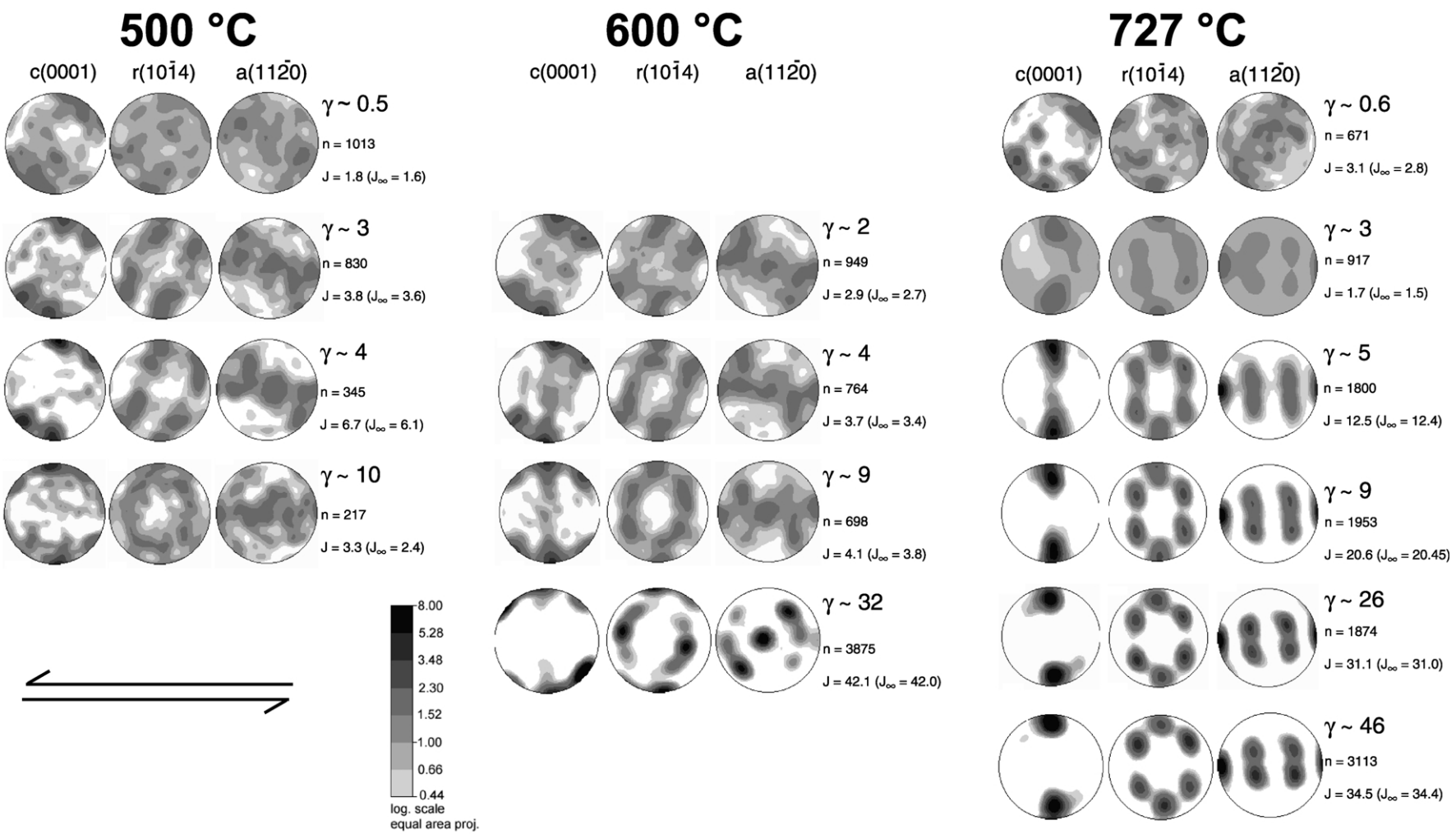

Fig. 7. CPO of samples deformed to various amounts of shear strain at different temperatures (500, 600 and 727 °C) and strain rates between 3.10^{-3} and 5.10^{-5} s^{-1}. The number of data points (n) corresponds to the number of grains measured by EBSD. Contoured pole figures (c, r and a) are processed using a Gaussian convolution with a half width of 15° and maximum expansion $L = 32$ within the harmonic calculus. CPO strength is indicated by the ODF texture index J and by the extrapolated texture index J_∞ for an infinite number of independent measurements: $J_\infty \approx J - (1/n)J_1$, where $J_1 = 200$ for trigonal crystal symmetry and a half width of 15° (Matthies and Wagner, 1996; Schmocker, 2002).

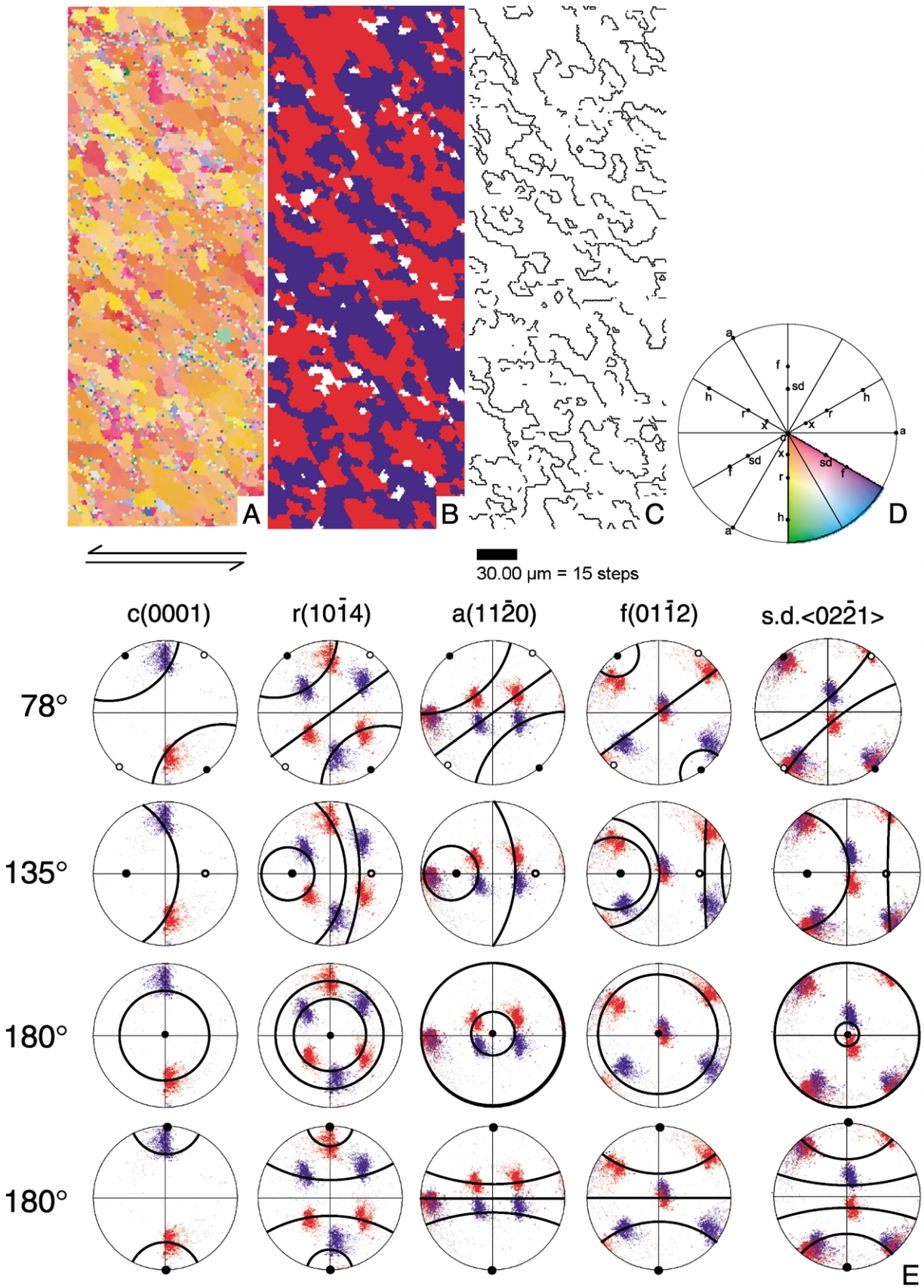
A
B
C
D
a
f
sd
h
r
x
30.00 μm = 15 steps
c(0001)
r(10$\bar{1}$4)
a(11$\bar{2}$0)
f(01$\bar{1}$2)
s.d.<02$\bar{2}$1>
78°
135°
180°
180°
E

under the experimental conditions of this study. Already at relatively small shear strains recovery processes are active and the hardening rate decreases with strain until peak stresses are reached. Because recovery processes are more efficient at higher temperatures, the amount of shear strain needed to reach the peak stress decreases with temperature ($\gamma = 2$ at 500 °C and $\gamma \leq 1$ at 727 °C and higher). Stress values remain at peak levels for at least another shear strain of one before weakening really starts, indicating a transitional phase of recovery-balanced dislocation creep. The start of weakening is observed to correspond to the onset of recrystallisation. The amount of weakening is moderate and seems to increase with temperature. Weakening occurs during dynamic recrystallisation of the large calcite grains (at $\gamma = 5$, >80% was recrystallised). Only in the high temperature experiments (727 °C in this study and 927 °C; see Pieri et al., 2001a,b) does weakening stop at larger strains, and stress values remain constant up to very large shear strains ($\gamma = 50$). A fully recrystallised ultramylonite results from deformation to $\gamma \geq 10$. Because the recovery processes are slower at 500 and 600 °C, slow weakening occurs until very large strains ($\gamma = 36$ at 600 °C) and constant stresses are not reached at these conditions. Remnants of the old large grains are still visible, although the sample has completely recrystallised to a fine-grained calcite ultramylonite. It is concluded that the major part of the weakening occurs during the transition from a deformation to a recrystallisation microstructure.

In the range of conditions covered by this study, the grain size reduction from a coarse-grained calcite marble to a fine-grained calcite mylonite is mainly caused by subgrain rotation recrystallisation. At very large strains ($\gamma = 29$ and 50, 727 °C), the bimodal distribution of the recrystallised grain size (mean values plotted in Fig. 6D) and the presence of a larger number of grains with irregular grain boundaries indicate an increase in activity of grain boundary migration recrystallisation with strain. Growth of the recrystallised grains by grain boundary migration and the formation of new subgrains cause a balance between rotation recrystallisation and grain boundary migration recrystallisation at large strain. It results in a constant bimodal grain size distribution and constant mean grain size during ongoing deformation and recrystallisation. The paleopiezometer obtained in this study (Fig. 8D) fits well with the paleopiezometer of Schmid et al. (1987) and the subgrain rotation paleopiezometer of Rutter (1995). In conclusion, although stable stress conditions are already obtained at $\gamma = 5$ (727 °C), the microstructure and CPO continuously evolve with further strain. Between $\gamma \sim 30$ and $\gamma \sim 50$ hardly any changes in stress level, deformation mechanisms, microstructure and CPO are observed. This would suggest that steady-state has been obtained, although a conclusive answer can only be given when the deformation behaviour is shown to be history independent, for instance by using different starting grain sizes. It is clear that much larger shear strains are needed to approximate steady-state conditions than those reached in compression tests or those postulated by Pieri et al. (2001a,b).

4.2. Dislocation creep versus diffusion creep

Strain rate stepping tests in the small strain regime show very high n-values ($n \geq 7$). The stress exponents remain high during weakening, after weakening and at very large shear strains. In addition, the microstructures indicate deformation by slip and climb of dislocations (see Section 4.1) and the strong CPOs suggest a high activity of various slip systems even at large strain (see Section 4.5). All these observations suggest that dislocation glide and creep are the dominant deformation mechanisms at all temperatures, even in the fully recrystallised ultramylonites. Although the grain size reduces by at least one order of magnitude, there are no indications for a switch in deformation processes from dislocation to diffusion creep or to some other grain size sensitive mechanism. Deformation mechanism maps constructed with flow laws for dislocation creep (Rutter, 1974; Schmid et al., 1980) and diffusion creep (Walker et al., 1990) would suggest a switch to the diffusion creep field due to grain size reduction at large shear strains in this study. However, none of the large strain studies (this study, Pieri et al., 2001a,b) show such transition for Carrara marble for strain rates $\geq 10^{-5}\ s^{-1}$ and temperatures ≤ 927 °C. Constructing deformation mechanism maps using flow laws determined for different materials (synthetic fine-grained versus natural coarse-grained Carrara marble) may not be appropriate. This also implies that the transition from diffusion to dislocation creep may not coincide with the recrystallised grain size paleopiezometer of Carrara marble. We would like to emphasize that diffusion creep (i.e. with stress exponents < 3) has been reported for hot-pressed aggregates of synthetic calcite (Walker et al., 1990; Herwegh et al., 2003), but not for Carrara marble.

Fig. 8. Detailed EBSD map with a stepsize of 2 μm of a Carrara marble sample deformed in torsion at 727 °C to $\gamma = 50$ at $2.10^{-3}\ s^{-1}$. (A) Orientation map of the raw data with colour key according to (D). (B) The data was filtered with an OIM smoothing routine in order to remove incorrectly indexed orientations, which were mostly located along grain boundaries. Two dominant orientations (each with a spread of 25°) are highlighted in red and blue on the map. The orientations of the white areas fall outside of this 25° spread. (C) Map highlighting boundaries with a misorientation of 78° around $\{1\bar{1}04\}$ in black (15° tolerance). (D) Colour key according to the inverse pole figure of normal to SZB. (E) Pole figures of the same data set with the two orientations highlighted as in (B). The misorientation axes between the two orientations are highlighted for each possible misorientation angle; the filled symbols are the rotation axes, lines correspond to the rotation path of the given pole or direction around the rotation axis. Open symbols represent the other rotation axes for the same angle, if applicable (curves indicating the rotation paths are not shown). The misorientation axes are listed in Table 3.

4.3. Dislocation creep flow laws

Several dislocation creep flow laws have been determined for calcite. Fig. 9 compares the mechanical data from this study with predictions from various calcite flow laws. The exponential and power-law creep rate equations determined by Rutter (1974) and Schmid et al. (1980), respectively, result in good fits for the torsion data at 727 °C, but at 500 °C higher strengths were measured than expected. Our complete data set could neither be fitted with a single exponential rate equation nor a single power-law rate equation. For similar reasons, De Bresser (2002) and Renner et al. (2002) proposed more sophisticated dislocation creep rate equations (dissociation controlled creep and a Peierls relation, respectively) to describe existing mechanical data for calcite. In contrast to standard power-law creep equations with constant stress exponents, these rate equations imply that the stress–strain rate relationship is dependent on temperature, with the intention to fit all the data over a larger temperature range. Since the focus of this paper is not the rheological behaviour of calcite but the interplay between rheology, microstructure and CPO, a determination of new rate equations for the torsion data was omitted. Fig. 9 shows both types of rate equations (De

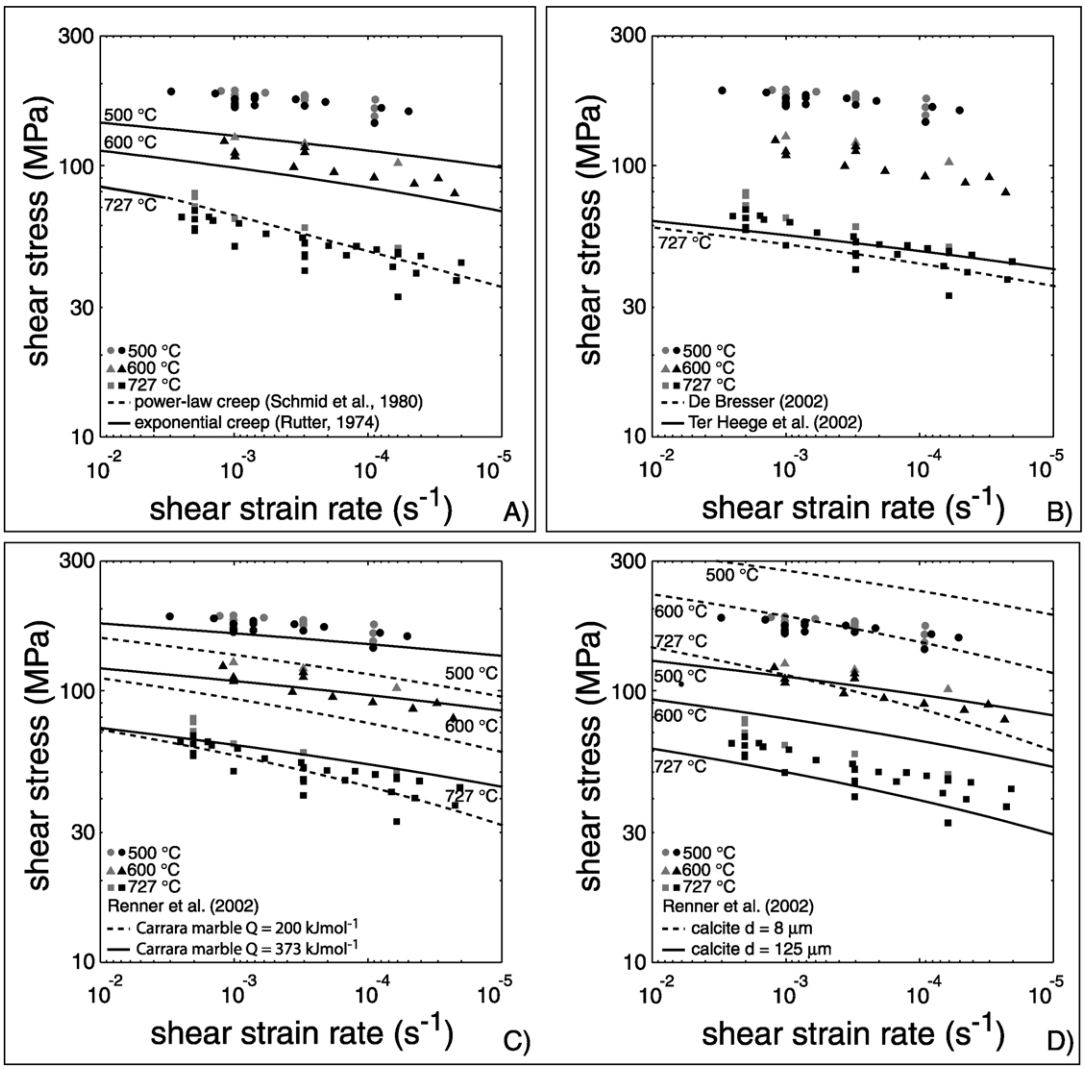

Fig. 9. Shear stress versus shear strain rate diagrams (log–log scale) for Carrara marble in the range of experimental conditions. Small strain ($\gamma < 2$) torsion data points are plotted in grey. Large strain torsion data points are plotted in black. (A) Solid lines are the exponential rate equations (500, 600 and 727 °C) of Rutter (1974). Dotted line is the power-law rate equation at 727 °C of Schmid et al. (1980). At each temperature and shear strain rate the active rate equation is shown (i.e. the one predicting the lowest shear stress at a given shear strain rate). (B) Cross-slip controlled rate equations for Carrara marble of De Bresser (2002) as thick dotted line and of Ter Heege et al. (2002) as thick solid line for 727 °C. The dissociation cross slip controlled rate equation is only valid for low stresses, therefore it is not plotted for high stresses (500 and 600 °C). (C) Peierls rate equations for Carrara marble of Renner et al. (2002) for 500, 600 and 727 °C. Solid lines represent the best-fit in the regression procedure for Carrara marble in their study ($Q = 373$ kJ mol^{-1}). Dotted lines represent the rate equations for Carrara marble obtained during regression with a fixed Q of 200 kJ mol^{-1}. (D) Peierls rate equation obtained by Renner et al. (2002) for calcite ($Q = 200$ kJ mol^{-1}) for 500, 600 and 727 °C. Solid lines are calculated for a grain size of 125 μm equivalent to the starting grain size of Carrara marble in this study. Dotted lines are for a grain size of 8 μm, equivalent to a mean recrystallised grain size of Carrara marble in this study. The equivalent stresses in the rate equations were converted to shear stresses following Schmid et al. (1987).

Bresser, 2002; Renner et al., 2002) in comparison with the torsion data.

The dissociation controlled cross slip rate equations determined by De Bresser (2002) and Ter Heege et al. (2002) fit the torsion data well at 727 °C, but predict much lower stresses for the lower temperatures (500 and 600 °C) due to the weak temperature dependence of the stress at these conditions. These rate equations have been determined from experiments at higher temperatures (700–1000 °C) than the temperatures used in this study. In addition, the published rate equations can only be applied at low stresses when $\sigma b/\gamma_s < 1$, where σ is the stress, b the Burgers vector and γ_s the stacking fault energy (De Bresser, 2002). This is valid for the torsion experiments at 727 °C, but $\sigma b/\gamma_s$ becomes close to one for the 500 and 600 °C experiments, and this rate equation should therefore not be applied at these low temperature/high stress conditions.

The Peierls rate equation for Carrara marble with an activation energy of 373 kJ mol^{-1} (Renner et al., 2002) and a fixed grain size of 200 μm best describes the torsion data (Fig. 9C). Based on a Hall–Petch relationship, this rate equation predicts an increase in stress with a decrease in grain size. While this grain size sensitivity in the rate equation may work well for large grain sizes (our small strain data), it cannot be used to describe the weakening in our large strain data, since it predicts an increase in strength with decreasing grain size (Fig. 9D). Therefore, new parameters or a new type of rate equation are needed to describe both small and large strain mechanical data for calcite. An attempt is made in Section 4.4 to include a descriptive parameter for the observed weakening into a rate equation.

4.4. Strain weakening

At all temperatures investigated, strain weakening starts at peak stress conditions after a critical strain (γ_{crit}), close to the onset of recrystallisation. At large strains, the weakening slows down and constant stresses are approached. The weakening can be correlated to the percentage of recrystallised grains as has also been observed in metals. Therefore, we have defined mechanical parameters to describe the weakening based on strain weakening models for dynamic recrystallisation in metals (Luton and Sellars, 1969). The amount of weakening can be estimated either as an average value (k) determined from small and large strain flow laws, or as a value (W) describing the amount of weakening in a specific experiment:

$$k = \frac{A_{\text{large strain}}}{A_{\text{peak}}} \text{ or } W = \frac{\tau_{\text{large strain}}}{\tau_{\text{peak}}} \quad (2)$$

where $A_{\text{large strain}}$ and A_{peak} are the small and large strain pre-exponential factors in the flow laws, and τ_{peak} and $\tau_{\text{large strain}}$ are the shear stress values at small and large strains in a single experiment. Following Luton and Sellars (1969), the shape of the weakening curve can be described by an exponential term $\exp(-a(\gamma - \gamma_{crit})^b)$ with two parameters a and b. The weakening can then be incorporated into the pre-exponential term A of the rate equation:

$$A = A_{\text{peak}}A(\gamma) = A_{\text{peak}}\left[k + (1-k)\exp(-a(\gamma - \gamma_{crit})^b)\right] \quad (3)$$

In the case of a power-law rate equation with a constant stress exponent n, an equivalent formulation is:

$$A = A_{\text{peak}}A(\gamma)$$
$$= A_{\text{peak}}\left[W^{-n} + (1 - W^{-n})\exp(-a(\gamma - \gamma_{crit})^b)\right] \quad (4)$$

These equations allow us to model weakening from the peak stress value towards an asymptotically approaching stable stress value. It differs from Rutter (1995) where the proposed weakening term causes the stress to approach zero at infinitely large strains.

Non-linear least square regression fitting of the weakening of all the experiments on Carrara marble to Eq. (4) resulted in best-fit estimates of a and b (Fig. 10D). Both variables vary slightly with temperature due to the difference in efficiency of recrystallisation. The average a and b values are about 0.1 and 2.5 for the range of conditions in this study. The obtained values for b are similar to $b = 2$ as observed in metals (Luton and Sellars, 1969). These parameters are only phenomenological descriptions of the weakening towards constant stresses. They are not linked yet to a physical process causing weakening, such as a change in activity of slip systems or a change in grain size.

De Bresser et al. (2001) proposed that grain size reduction and weakening in large strain microstructures result from a competition between grain size sensitive and grain size insensitive mechanisms. For the 20% weakening and $n = 8$ obtained in this study, they predict an 80% contribution of grain size sensitive mechanisms to the deformation. Although it cannot be excluded that grain size sensitive mechanisms were active to some extent, the very strong CPOs, abundant subgrain formation at large strains and the development of the secondary foliation suggest that dislocation creep processes continue to dominate also at large strains.

4.5. CPO

Two distinct large strain CPOs develop at low (500 and 600 °C) and high temperatures (727 °C). The difference in the evolution of the CPO with strain is interpreted to be caused by the activity of different slip systems during recrystallisation.

At small shear strains recrystallisation has not started (e.g. $\gamma = 6$ at 500 °C and $\gamma = 2$ at 727 °C) and a CPO forms with {r}⟨s.d.⟩ and {c}⟨a⟩ orientation components (⟨s.d.⟩ = $\langle 02\bar{2}1\rangle$, shear direction) at all temperatures. This CPO type

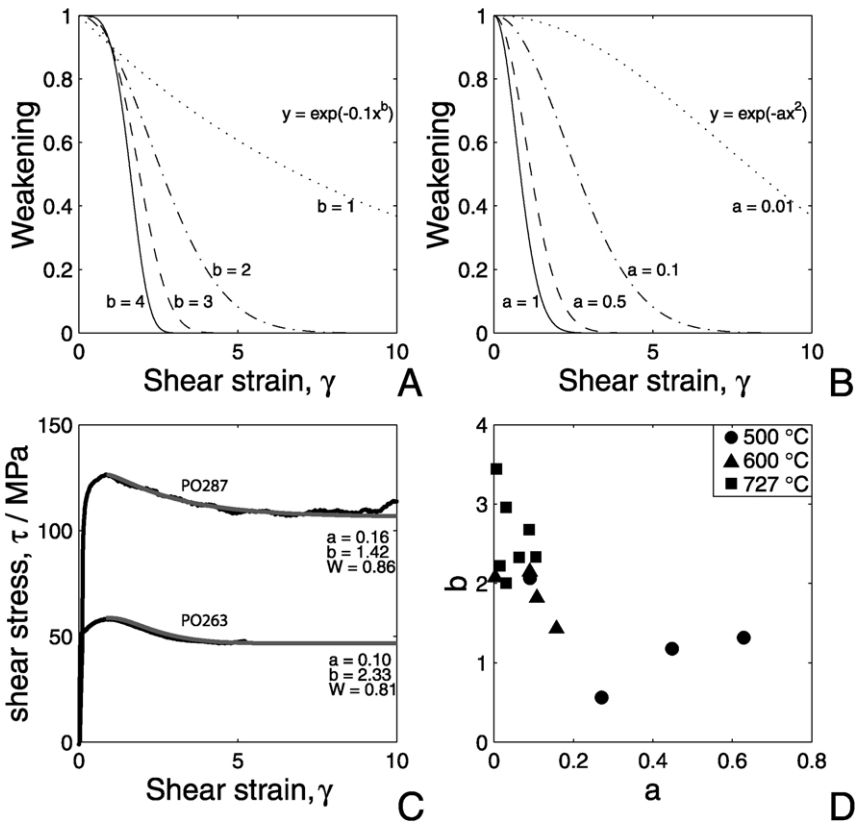

Fig. 10. Diagrams showing the weakening term in Eqs. (3) and (4). (A) and (B) Effect of varying the constants a and b, respectively, in the weakening term. (C) Modelled weakening curve for two large strain experiments (PO287, $\gamma = 10$ at 600 °C and PO263, $\gamma = 5$ at 727 °C). The black curve represents the experimental data. The grey curve represents the modelled weakening (Eq. (4)). (D) Plot of the weakening parameters a and b obtained for each experiment by a non-linear regression procedure of Eq. (4).

has been observed in other experimental studies on calcite (e.g. Schmid et al., 1987; Pieri et al., 2001a,b) and in naturally deformed calcite rocks (e.g. Behrmann, 1983; Dietrich and Song, 1984; Ratschbacher et al., 1991). It is commonly called a deformation CPO and is extensively used as a shear sense indicator in natural calcite mylonites with a c-axis maximum inclined against the direction of shear. Numerical simulations of CPO development reproduce this CPO when multiple slip system activity is enforced by strain compatibility requirements (Wenk et al., 1987; Pieri et al., 2001b).

Dynamic recrystallisation changes the CPO significantly. At 500 and 600 °C and large shear strains, a third c-axis maximum develops exactly opposite to one of the $\{r\}\langle s.d.\rangle = \{10\bar{1}4\}\langle 20\bar{2}\bar{1}\rangle$ maxima at small strains. This new component $\{10\bar{1}4\}\langle\bar{2}021\rangle$ becomes stronger at very large shear strains ($\gamma = 36$ at 600 °C) and starts to replace the two previous maxima. Glide along the $\{10\bar{1}4\}\langle\bar{2}021\rangle$ slip system appears to be more favourable during recrystallisation than along the $\{10\bar{1}4\}\langle 20\bar{2}\bar{1}\rangle$ slip system (favoured at small shear strains). This reflects that slip on the same slip system may be activated with different ease in the two opposite senses. A CPO with all three maxima has been reported by Schmid et al. (1987) and has been discussed by Casey et al. (1998), although a change in maxima strength at large strains was not observed.

At the higher temperatures (727 °C and higher) a recrystallisation CPO is formed at large strains with a strong orientation component aligned between $\{c\}\langle a\rangle$ and $\{r\}\langle a\rangle$. Pieri et al. (2001b) proposed a new slip system $\{r\}\langle a\rangle$ to explain their Carrara marble CPO observations. Careful analysis of our results at the largest shear strains ($\gamma = 26$ and $\gamma = 46$) shows that the strong single maxima are not perfectly aligned in a $\{r\}\langle a\rangle$ orientation (corresponding to an angle of 45° of the c-axes to the SZB normal), but deviate $\sim 20°$ equally from the ideal $\{r\}\langle a\rangle$ and the $\{c\}\langle a\rangle$ orientations. Since these maxima are not oriented in an easy-slip orientation, several slip systems are likely to operate simultaneously. Although microstructure and strength do not evolve anymore after $\gamma \sim 10$, the CPO continues to strengthen with increasing strain. At large shear strains ($\gamma = 26$ and $\gamma = 46$ at 727 °C), the oblique tail of orientations aligned with the sense of shear and next to the maxima can be explained by a balance between rotation and migration recrystallisation. As some grains rotate a bit away from the dominant orientations with the c-axes perfectly normal to the shear direction, other slip systems must be activated during ongoing deformation. This leads to

subgrains and eventually grains in harder orientations, which will be rapidly consumed by other grains in the dominant orientations through grain boundary migration. Rotation and consumption by grain boundary migration is probably fast, since only a small number of grains have orientations away from the dominant orientation. The process of continuous rotation and consumption forms a steady microstructure at large strains and explains the small asymmetry of the CPO.

In general, the overall reduction in asymmetry of the CPO at all temperature conditions with increasing shear strain indicates that CPO alone is ambiguous as a shear sense indicator. Additional microstructural features need to be present to be able to infer a shear sense from a calcite mylonite. On the other hand, the combined study of microstructures and CPO can be used to constrain the range of deformation conditions (temperature, amount of shear strain) in natural shear zones.

4.6. Secondary foliation

The development of a strong secondary foliation oblique with respect to the primary foliation and the SZB is caused by grain boundary alignment of the recrystallised grains during recrystallisation. The high resolution EBSD map of the sample deformed to $\gamma = 50$ at 727 °C indicates that grain boundaries between two groups of crystal orientations (highlighted in blue and red in Fig. 8B and E) form the secondary foliation. The orientation of the second foliation is constant across the thin section and remains stable irrespective of strain, but is steeper at higher temperatures than at lower temperatures. Six different pairs of misorientation axes and angles are possible for these special grain boundaries (Table 3). For the set with the smallest misorientation angle (78° around $(1\bar{1}04)$) the rotation axis is parallel to the secondary foliation. The secondary foliation may be parallel to one of the {f} planes assuming that it is vertical to the section plane. This possible correlation to a specific crystallographic plane could explain the relatively high angle orientation (>45°) of the secondary foliation. A similar interpretation was also suggested by Lister and Snoke (1984) for high angle foliations in quartz mylonites.

During deformation in simple shear, any line should rotate passively towards the SZB. Recrystallisation occurs locally, but is continuously active throughout the sample. Multiple cycles of recrystallisation continuously reset the rotated secondary foliation towards its original steep orientation. This is evidenced by the absence of lower angle secondary foliations (<30° with SZB) and by a small angular spread (maximum of 15°) of the secondary foliation (mean orientation is 50° with SZB). For instance, a rotation of the foliation from 50 to 20° occurs after an additional shear strain of one or two (Fig. 11). Therefore, between $\gamma = 10$ (first occurrence of secondary foliation) and $\gamma = 50$ (largest strain experiment at 727 °C), approximately 20

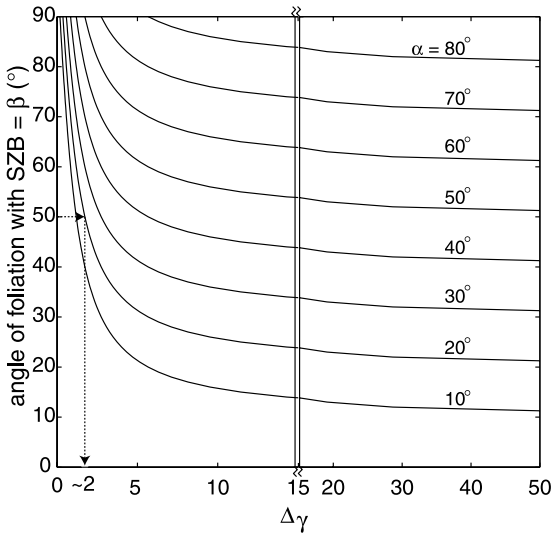

Fig. 11. Rotation of planar markers in simple shear. Continuous deformation will result in the passive rotation of a foliation towards the SZB following ($\gamma = \tan(90 - (\alpha - \beta))$), where α is the rotation angle and β the original angle of the foliation with the shear zone boundary (SZB). For example, the arrows indicate that a foliation with an original orientation of 50° with SZB will rotate 20° during an additional shear strain of ~2.

recrystallisation cycles are estimated to have occurred. The lower angle secondary foliations in the low temperature experiments (500 and 600 °C) may correspond to slower cycles of recrystallisation.

The first and secondary foliations from our experiments closely resemble S–C fabrics observed in quartz mylonites (Lister and Snoke, 1984), which were interpreted to have formed due to cyclic recrystallisation. S–C fabrics were also reported in calcite mylonites on Thassos Island, Greece (Bestmann et al., 2000) and in the Bancroft shear zone, Canada (Van der Pluijm, 1991; Busch and van der Pluijm, 1995). Law et al. (1984) proposed that oblique foliations are indicative of steady-state foliations. Herwegh and Handy (1998) reported a similar formation of oblique foliation in 'see-through' experiments on norcamphor. The observation of continuous resetting towards a steep secondary foliation after small rotation increments confirms the idea that cyclic recrystallisation helps to maintain stable oblique foliations.

The observed secondary foliation serves as an excellent shear sense indicator. In addition, the angle between the C- and S-surfaces can be used as a measure indicating the relative rates of rotation (through deformation) and resetting (through recrystallisation, temperature-dependent). The presence of a secondary foliation suggests large strain deformation and cyclic dynamic recrystallisation processes. However, the secondary foliation cannot be used to estimate the total amount of strain. The secondary foliation may completely overprint the primary foliation at very large shear strains. This may cause a misinterpretation of the strain field in natural mylonites, when the second foliation is

mistakenly thought to be of primary origin. Additional information about mylonites at a larger scale, such as the orientation of the shear zone boundary, can help avoid such ambiguities.

5. Conclusions

- Carrara marble was experimentally deformed in torsion up to very large shear strains ($\gamma \leq 50$) at different temperatures and constant strain rates. Deformation remained in the dislocation creep field even up to the largest shear strain. No evidence was found for any significant contribution from diffusive processes.
- Recrystallisation started at moderate shear strain ($\gamma \sim 1$) and was accompanied by strain weakening until most of the microstructure was completely recrystallised. The weakening was followed by approximately constant stress values during ongoing dynamic recrystallisation cycles by both subgrain rotation and grain boundary migration.
- During recrystallisation two different CPOs developed depending on temperature, suggesting that recrystallisation activated different slip systems at different temperatures. At very large shear strains the CPO showed an obliquity opposite to the non-recrystallised small strain obliquity. This change in obliquity can lead to misinterpretation of the applied sense of shear if no other information on the strain history is available (e.g. evidence of dynamic recrystallisation or secondary foliation).
- Due to continuous dynamic recrystallisation an oblique secondary foliation formed at large strains. At 727 °C the orientation of the secondary foliation is crystallographically controlled and stable with strain. It indicates the efficiency of recrystallisation relative to deformation and can be used as a relative thermometer (for similar strain rates). At very large strains the secondary foliation overprints the initial foliation, which can result in misinterpretation of the geometry of the applied strain/stress field if first and secondary foliations are misidentified.
- At 727 °C, constant stress levels, deformation mechanisms, microstructure and CPO indicate that steady-state may have been approached at the largest strains. However, it still needs to be confirmed that the large strain behaviour is independent of the deformation history. At lower temperatures, steady-state has clearly not been achieved even at shear strains of 36.
- At large strains the material looses most of the microstructural and CPO features that allow evaluation of the amount of applied shear strain. In nature, a mylonite with a strong CPO but without any information on the amount of strain would indicate that large strains were imposed.

Acknowledgements

Nils Oesterling and Marco Herwegh are thanked for stimulating discussions. We thank Jean-Pierre Burg for his support and constructive comments. Frowin Pirovino is acknowledged for preparing excellent ultra-thin sections. Steve Covey-Crump and Hans de Bresser are gratefully acknowledged for their constructive reviews as well as Tom Blenkinsop for additional editorial comments. David Olgaard and Mervyn Paterson are thanked for installing the torsion apparatus. We are indebted to Stefan Schmid since preliminary experiments at lower temperatures and strain rates conducted together with him in our laboratory were a source of inspiration for this experimental study. This study was supported by ETH project No. 00744/41-2704.5 and Swiss Nationalfond project No. 2-77010-00.

References

Adams, B.L., Wright, S.I., Kunze, K., 1993. Orientation imaging: the emergence of a new microscopy. Metallurgical Transactions 24A (4), 819–830.

Behrmann, J.H., 1983. Microstructure and fabric transitions in calcite tectonites from the Sierra Alhamilla (Spain). Geologische Rundschau 72, 605–618.

Bestmann, M., Kunze, K., Matthews, A., 2000. Evolution of a calcite marble shear zone complex on Thassos Island, Greece: microstructural and textural fabrics and their kinematic significance. Journal of Structural Geology 22, 1789–1807.

Burkhard, M., 1993. Calcite twins, their geometry, appearance and significance as stress-strain markers and indicators of tectonic regime: a review. Journal of Structural Geology 15, 351–368.

Busch, J.P., van der Pluijm, B.A., 1995. Calcite textures, microstructures and rheological properties of marble mylonites in the Bancroft shear zone, Ontario, Canada. Journal of Structural Geology 17, 677–688.

Bystricky, M., Kunze, K., Burlini, L., Burg, J.-P., 2000. High shear strain of olivine aggregates: rheological, textural and seismic consequences. Science 290, 1564–1567.

Casey, M., Kunze, K., Olgaard, D.L., 1998. Texture of Solnhofen limestone deformed to high strains in torsion. Journal of Structural Geology 20, 255–267.

Covey-Crump, S.J., 1994. The application of Hart's state variable description of inelastic deformation to Carrara marble at $T < 450$ °C. Journal of Geophysical Research 99 (B10), 19793–19808.

De Bresser, J.H.P., 2002. On the mechanism of dislocation creep of calcite at high temperature: inferences from experimentally measured pressure sensitivity and strain rate sensitivity of flow stress. Journal of Geophysical Research 107 (B12), 2337 DOI: 10.1029/2002JB001812.

De Bresser, J.H.P., Ter Heege, J.H., Spiers, C.J., 2001. Grain size reduction by dynamic recrystallisation: can it result in major rheological weakening? International Journal of Earth Sciences 90, 28–45.

Dietrich, D., Song, H., 1984. Calcite fabrics in a natural shear environment, the Helvetic nappes of Switzerland. Journal of Structural Geology 6, 19–32.

Griggs, D.T., Turner, F.J., Heard, H.C., 1960. Deformation of rocks at 500–800 °C. Memoirs of the Geological Society of America 79, 39–105.

Handin, J., Higgs, D.V., O'Brien, J.K., 1960. Torsion of Yule marble under confining pressure. Memoirs of the Geological Society of America 79, 245–274.

Heidelbach, F., Stretton, I.C., Kunze, K., 2001. Texture development of polycrystalline anhydrite deformed in torsion. International Journal of Earth Sciences 90, 118–126.

Heidelbach, F., Stretton, I., Langenhorst, F., Mackwell, S., 2003. Fabric evolution during high shear strain deformation of magnesiowüstite ($Mg_{0.8}Fe_{0.2}O$). Journal of Geophysical Research 108 (B3), 2154 DOI: 10.1029/2001JB001632.

Herwegh, M., Handy, M.R., 1998. The origin of shape preferred orientations in mylonite: inferences from in-situ experiments on polycrystalline norcamphor. Journal of Structural Geology 20, 681–694.

Herwegh, M., Xiao, X., Evans, B., 2003. The effect of dissolved magnesium on diffusion creep of calcite. Earth and Planetary Science Letters 212, 457–470.

Law, R.D., Knipe, R.J., Dayan, H., 1984. Strain path partitioning within thrust sheets: microstructural and petrofabric evidence from the Moine Thrust zone at Loch Eriboll, Northwest Scotland. Journal of Structural Geology 6, 477–497.

Lister, G.S., Snoke, A.W., 1984. S–C mylonites. Journal of Structural Geology 6, 617–638.

Luton, M.J., Sellars, C.M., 1969. Dynamic recrystallisation in nickel and nickel–iron alloys during high temperature deformation. Acta Metallurgica 17, 1033–1043.

Matthies, S., Wagner, F., 1996. On a 1/*n* law in texture related single orientation analysis. Physica Status Solidi B-Basic Research 196 (2), K11–K15.

Panozzo Heilbronner, R., 1992. The autocorrelation function: an image-processing tool for fabric analysis. Tectonophysics 212, 351–370.

Paterson, M.S., Olgaard, D.L., 2000. Rock deformation tests to large shear strains in torsion. Journal of Structural Geology 22, 1341–1358.

Pieri, M., Burlini, L., Kunze, K., Olgaard, D.L., Stretton, I.C., 2001a. Rheological and microstructural evolution of Carrara marble with high shear strain: results from high temperature torsion experiments. Journal of Structural Geology 23, 1393–1413.

Pieri, M., Kunze, K., Burlini, L., Stretton, I.C., Olgaard, D.L., Burg, J.-P., Wenk, H.R., 2001b. Texture development of calcite by deformation and dynamic recrystallisation at 1000 K during torsion experiments of marble to large strains. Tectonophysics 330, 119–140.

Prior, D.J., 1999. Problems in determining the misorientation axes, for small angular misorientations, using electron backscatter diffraction in the SEM. Journal of Microscopy 195, 217–225.

Renner, J., Evans, B., Siddiqi, G., 2002. Dislocation creep of calcite. Journal of Geophysical Research 107 (B12), 2364DOI: 10.1029/2001JB001680.

Ratschbacher, L., Wenk, H.R., Sintubin, M., 1991. Calcite textures: examples from nappes with strain-partitioning. Journal of Structural Geology 13, 369–384.

Rutter, E.H., 1974. The influence of temperature, strain rate and interstitial water in the experimental deformation of calcite rocks. Tectonophysics 22, 311–334.

Rutter, E.H., 1995. Experimental study of the influence of stress, temperature and strain on the dynamic recrystallisation of Carrara marble. Journal of Geophysical Research 100, 24651–24663.

Rutter, E.H., 1998. Use of extension testing to investigate the influence of finite strain on the rheological behaviour of marble. Journal of Structural Geology 20, 243–254.

Rutter, E.H., Casey, M., Burlini, L., 1994. Preferred crystallographic orientation development during the plastic and superplastic flow of calcite rocks. Journal of Structural Geology 16, 1431–1446.

Schmid, S.M., Boland, J.N., Paterson, M.S., 1977. Superplastic flow in fine grained limestone. Tectonophysics 43, 257–291.

Schmid, S.M., Paterson, M.S., Boland, J.N., 1980. High temperature flow and dynamic recrystallisation in Carrarra marble. Tectonophysics 65, 245–280.

Schmid, S.M., Panozzo, R., Bauer, S., 1987. Simple shear experiments on calcite rocks: rheology and microfabric. Journal of Structural Geology 9, 747–778.

Schmocker, M., 2002. Rheology and microfabrics of quartz: experimental deformation in torsion. Dissertation ETH Nr. 14587, 197pp.

Schmocker, M., Bystricky, M., Kunze, K., Burlini, L., Stünitz, H., Burg, J.-P., 2003. Granular flow and Riedel band formation in water-rich quartz aggregates experimentally deformed in torsion. Journal of Geophysical Research 108 (B5), 2242 DOI: 10.1029/2002JB001958.

Ter Heege, J.H., De Bresser, J.H.P., Spiers, C.J., 2002. The influence of dynamic recrystallisation on the grain size distribution and rheological behaviour of Carrara marble deformed in axial compression. In: De Meer, S., Drury, M.R., De Bresser, J.H.P., Pennock, G.M. (Eds.), Deformation Mechanisms, Rheology and Tectonics: Current Status and Future Perspectives. Geological Society of London, Special Publications 200, pp. 331–353.

Van der Pluijm, B.A., 1991. Marble mylonites in the Bancroft shear zone, Ontario, Canada: microstructures and deformation mechanisms. Journal of Structural Geology 13, 1125–1135.

Venables, J.A., Harland, C.J., 1973. Electron back-scattering patterns—a new technique for obtaining crystallographic information in the scanning electron microscope. Philosophical Magazine 27, 1193–1200.

Walker, A.N., Rutter, E.H., Brodie, K.H., 1990. Experimental study of grain-size sensitive flow of synthetic, hot-pressed calcite rocks. In: Knipe, R.J., Rutter, E.H. (Eds.), Deformation Mechanisms, Rheology and Tectonics. Geological Society of London, Special Publications 54, pp. 259–284.

Wenk, H.R., 1985. Carbonates. In: Preferred Orientation in Deformed Metals and Rocks. An Introduction to Modern Texture Analysis, Academic Press, pp. 361–384.

Wenk, H.R., Takeshita, T., Bechler, E., Erskine, B.G., Matthies, S., 1987. Pure shear and simple shear calcite textures. Comparison of experimental, theoretical and natural data. Journal of Structural Geology 9, 731–745.

Wenk, H.R., Matthies, S., Donovan, J., Chateigner, D., 1998. BEARTEX, a Windows-based program system for quantitative texture analysis. Journal of Applied Crystallography 31, 262–269.